Ag/ZnO flower heterostructures as a visible-light driven photocatalyst via surface plasmon resonance

Zhizhong Han [a], Lili Ren [a], Zhihui Cui [a], Chongqi Chen [a,b], Haibo Pan [a,*], Jianzhong Chen [a,**]

[a] College of Chemistry and Chemical Engineering, Qishan Campus, Fuzhou University, Fuzhou, Fujian 350108, China
[b] National Engineering Research Center of Chemical Fertilizer Catalyst, Fuzhou University, Fuzhou, Fujian 350002, China

ARTICLE INFO

ABSTRACT

Visible-light driven photocatalyst, Ag/ZnO flower (ZnO Fl) heterostructures, was prepared on indium doped tin oxide (ITO) glass via a simple photoreduction method without surfactants. The samples are characterized by X-ray diffraction, scan electron microscopy, X-ray photoelectron spectroscopy, UV–vis spectroscopy, photoluminescence spectra and photocurrent response. The results show that ZnO FRs are wurtzite phase with single crystalline grown along the [0 0 1] direction and Ag nanoparticles (NPs) located on the surface are metallic. The binding energy of Ag 3d for the Ag/ZnO Fls sample shifts remarkably to the lower binding energy compared with the corresponding value of pure metallic Ag attribute to the interaction between Ag and ZnO Fls. Ag/ZnO Fl heterostructures exhibit higher visible-light driven photocatalytic activity. It is suggested that photo-induced electrons are generated from Ag due to surface plasmon resonance, and transfer from Ag to ZnO Fls. Then the electrons interact with adsorbed oxygen, finally forming hydroxyl radicals (•OH), and the visible-light driven photocatalytic efficiency is enhanced. The proposed mechanism is further confirmed by the photoluminescence and transient photocurrent response. Additionally, the as-prepared Ag/ZnO Fls/ITO as a convenient photocatalytic device can be recycled without centrifugation.

1. Introduction

During the past decades, environmental problems such as air and water pollution has become a block for economic development and human health, therefore, it also have provide impetus for sustained fundamental and applied research in the area of environmental remediation. And the semiconductor metal oxides, such as TiO₂ and ZnO, have been found potential application in photocatalysis [1–3]. ZnO is a wide-direct gap semiconductor with a high exciton binding energy of 60 meV and band gap energy of 3.3 eV at room temperature [4], and its photodegradation mechanism has been proven to be similar to that of TiO₂ [5]. Therefore, ZnO can be regarded as a promising photocatalytic material in the ultraviolet spectral range and are widely applied in recent years [6–9]. Whereas the major factor of affecting the photocatalytic efficiency of ZnO is the recombination of photo-generated electron–hole pairs. The photo-generated electron–hole pairs recombine rapidly within or at the surface of ZnO particles, and this brings about a low quantum efficiency, which results in the low photocatalytic efficiency of the ZnO structure systems. Another limitation

to achieving high photocatalytic efficiency for ZnO is the narrow absorption spectral range, which is about 3–5% of total solar irradiance, since only UV light can be absorbed by pure ZnO nanoparticles (NPs).

To address these issues, the rational design of photocatalytic systems should allow efficient charge separation, transport, and utilization to obtain excellent photocatalytic quantum efficiency [10]. The novel photocatalysts of metal Ag hybridized with semiconductor is recognized as a promising candidate photocatalytic system. First, deposition of metal Ag NPs with a large work function (4.26 eV) onto photocatalysts surface has been found to efficiently impede the recombination of photo-generated electron–hole pairs because of the Schottky barrier formed at the metal–semiconductor interface [11]. And the transition metal ions can improve the electron scavenging mechanism, which is attributed to their behavior as electron scavengers via $M^{n+} + e_{cb}^- \rightarrow M^{(n-1)+}$, where e_{cb} is the photo-induced electron [12]. Thus, the separation of photo-generated electron–hole pairs is enhanced. Second, Ag is well known for its intense interactions with visible-light via the resonance of the oscillations of the free electrons within the particles [13]. Currently, visible-light driven plasmonic photocatalysts have been considered as one of the most potential alternatives to the traditional photocatalysts [14–17]. Additionally, silver also has the highest electrical and thermal conductivity among all metals, which makes it an ideal component for electrical interconnection

---

* Corresponding author. Tel.: +86 591 22866127; fax: +86 591 22866127.
** Corresponding author.
   E-mail addresses: hbpan@fzu.edu.cn (H. Pan), j.z.chen@fzu.edu.cn (J. Chen).
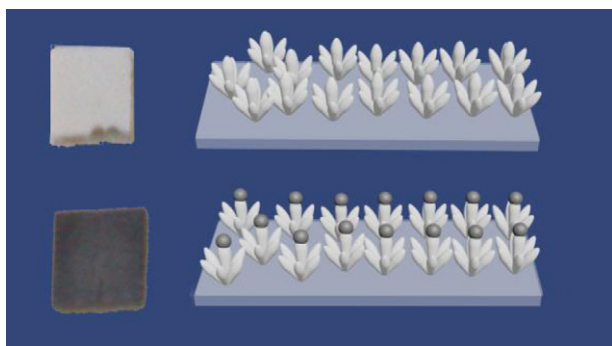
Fig. 1. Practical and schematic structures of ZnO Fls and Ag/ZnO Fls.

[18]. Methods including sonochemical synthesis [19], in situ reduction [20], deposition–precipitation [21], sol–gel process [22], and photochemical solution deposition [23] have been used to successfully synthesize the Ag/ZnO nanocrystal. In this work, Ag NPs were prepared though a facile photoreduction method [24–28]. In the photocatalytic reduction processes, Ag^+ ions capture the electrons from excited ZnO nanoparticles under UV irradiation, and then Ag NPs are formed. Therefore, it does not need an additive reductant in the process.

Implementing Ag nanostructures at specific locations to trap more light and/or localize it for the optimal generation of electrical energy is an interesting and important area of research. To authors' best knowledge, although Ag/ZnO heterostructures have been extensively studied in many respects as described above, there has still no report about the architectures of Ag/ZnO flowers (Fls) based on ITO. The oriented ZnO 3D (flower) structures have a higher areal proportion of exposed (0 0 1) faces, which are active crystal faces, and can enhance the photocatalytic activity [29]. In our work, the Ag/ZnO Fls were synthesized for two steps as Fig. 1 show: First, the ZnO Fls were built on ITO, and they displayed white (left of Fig. 1). Then Ag grew on ZnO Fls and samples became gray-brown. The as-prepared ZnO FRs/ITO is used as a photocatalytic device, which is convenient to recycle without centrifugation. The Ag/ZnO heterostructured nanofibers prepared by Lin et al. [2] could not absorb visible-light, thus, the visible-light-induced degradation of Rhodamine B (RhB) in their work is poor and neglectable. However, in our work, the as-prepared Ag/ZnO Fls display an efficient photodegradation of RhB under visible-light irradiation. In addition, the photo-generated currents density, photo-induced behavior, and charge transfer are also investigated using electrochemical methods. The results disclose surface and interface structures of the prepared samples, and then the photodegradation mechanism is induced in detail.

2. Experimental

2.1. Preparation of Ag/ZnO Fl heterostructures on ITO

To prepare Ag/ZnO Fl heterostructures, oriented ZnO Fls were firstly grown on ITO substrates (Heptachroma Solar Tech., 15 Ω/sq). Before the ZnO Fls growth, the substrates were cleaned by sonication in detergent, acetone, ethanol, and deionized water, and then dried in an oven. The substrates were then seeded by spin coating (1000 rpm, 50 s) with 6 mM zinc acetate dihydrate ($Zn(Ac)_2 \cdot 2H_2O$, 99%, Sino Chem. Reagent, 5 mM) in ethanol, followed by thermal decomposition at 300 °C for 20 min. The seeded substrates were placed in an aqueous solution containing 39 mM zinc nitrate hexahydrate ($Zn(NO_3)_2 \cdot 6H_2O$, 99%, Sino Chem. Reagent, 25 mM), 12.5 mM hexamethylenetetramine (HMTA, 99%, Sino Chem. Reagent), 5 mM polyethylenimine (PEI, 99%, Aladdin

Reagent), and 0.35 M ammonium hydroxide ($NH_3 \cdot H_2O$, 25–28%, Sino Chem. Reagent) at 87 °C for 3–4 h. Finally, the ZnO samples were dried in air.

The Ag loaded ZnO Fl or ZnO NP (Alfa Aesar) heterostructures were prepared with a photoreduction treatment method. Briefly, the as-prepared ZnO Fls or ZnO NPs were immerged into 0.5 M $AgNO_3$ aqueous solution (350 mg/10 mL) in a quartz flask. Then they were irradiated with a xenon lamp (50 W, HSX-F/UV 300, NBeT Group Corp.) for 0.5 h. The resulting Ag/ZnO Fl or ZnO NPs heterostructures were rinsed with deionized water several times, and dried at room temperature in the dark. Finally, the samples were calcined at 450 °C for 0.5 h.

2.2. Material characterizations

Crystalline structures of Ag/ZnO Fls were analyzed by powder X-ray diffraction (XRD, X'pert, Philips, Holland). Surface morphologies of the samples across the entire substrate were characterized by field-emission scanning electron microscopy (FE-SEM, Hitachi S4800, Japan), while the transmission electron microscope (TEM, Tecnai G2 F20 S-TWIN, 200 kV, FEI, USA) was used to examine the morphology of Ag/ZnO Fls. The UV–vis absorption and diffuse reflectance spectra were measured on a Perkin-Elmer Lambda 900 spectrophotometer. The photoluminescence (PL) spectra were recorded at room temperature employing a Cary Eclipase (Varian, USA). For PL measurement, the ZnO Fls and Ag/ZnO Fls were removed from the ITO. Then ZnO Fls and Ag/ZnO Fls were dispersed in distilled water, and obtained at the same concentration for them. The surface properties of samples were characterized by X-ray photoelectron spectroscopy (XPS) in a PHI Quantum 2000 Scanning ESCA Microprobe (PHI. Corp., USA) system with a monochromatic Al $K\alpha_{1,2}$ source (1486.60 eV). All binding energies were referenced to the C1s peak at 284.8 eV of the surface adventitious carbon. Except for FE-SEM characterizing, ZnO Fls and Ag/ZnO Fls were scraped off from the ITO with a blade.

2.3. Photoelectrochemical and photocatalytic measurements

The electric properties of the samples were performed with an electrochemical workstation (CHI 660D, CH Instrument Company, China). All electrochemical analyses were executed using a conventional three-electrode system. The working electrode was an as-prepared Ag/ZnO Fls/ITO or ZnO Fls/ITO created through spin coating. A platinum wire and a saturated Ag/AgCl electrode were used as a counter and a reference electrode, respectively. The electrolyte solution was 0.1 M Na_2SO_4 solution and RhB aqueous solution with a concentration of 5 μM. The Na_2SO_4 solution was used as the supporting electrolyte.

For photocatalytic measurement, the device of Ag/ZnO Fls/ITO or Ag/ZnO NPs/ITO created through spin coating (2 cm × 2 cm) was immersed into 50 mL RhB aqueous solution (5 μM), and was subsequently irradiated using a xenon lamp within 390–770 nm. Then at a definite time interval, 4 mL samples were withdrawn for analysis using a UV-vis spectrophotometer (PE Lambda 900). The degradation efficiency was defined as $\eta = (1 - C/C_0) \times 100\%$, where C and C_0 were the equilibrium concentration of RhB after and before visible-light irradiation. And the concentration of RhB was linear proportion to absorption (A), thus $C/C_0 = A/A_0$.

3. Results and discussion

3.1. Crystal structure and morphology

The XRD patterns of the as-prepared samples are shown in Fig. 2. Three distinct peaks at 31.8°, 34.4°, and 36.3° are observed in both
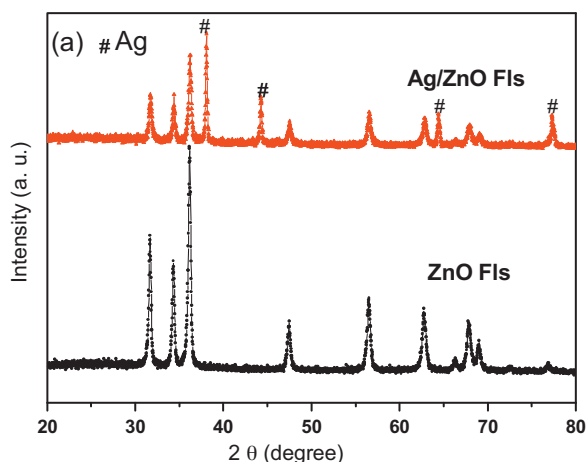
Fig. 2. XRD patterns of ZnO Fls and Ag/ZnO Fls. (For interpretation of the references to color in this figure, the reader is referred to the web version of this article.)

patterns, which are representing (1 0 0), (0 0 2), and (1 0 1) ZnO crystal planes. It is assigned to pure wurtzite ZnO phase denoting P6₃mc space group as cross-referenced to JCPDS 36-1451 card. While those of 38.2°, 44.4°, 64.6° and 77.5° can be indexed to fcc metallic Ag (marked with #, JCPDS 04-0783). The peaks corresponding to AgO and Ag_2O are not detected [30]. Additionally, there is no notable shift of all diffraction peaks between the two samples, revealing that no $Zn_{1-x}Ag_xO$ solid solution is formed and lattice expansion and/or shrinkage of Ag/ZnO nanocrystals should be negligible.

In order to describe the morphologies of ZnO Fls and the distribution of Ag NPs on the surface of ZnO Fls in the as-prepared Ag/ZnO Fls, SEM and TEM observation were carried out. Fig. 3a and b shows the SEM images of ZnO Fls. It can be found in Fig. 3b that

the ZnO Fls are formed by cone-like building blocks. The exposed crystal faces were mainly composed of (1 0 0) and (0 0 1) planes. As shown in Fig. 3c, there are a great amount of spherical Ag particles and ZnO Fls, suggesting that the microstructure of Ag/ZnO Fls is almost maintained after Ag deposition (inset of Fig. 3c). Moreover, Fig. 3c displays that the Ag NPs are uniformly dispersed, which is in good agreement with the XRD results. Fig. 3d shows a TEM image of Ag/ZnO Fls, where two Ag NPs (in the circle marked blue) attach to a ZnO Fls. For obtaining the value of lattice spacing for Ag/ZnO Fls, we choose two smaller Ag NPs, and a bigger one is also shown in the left inset of Fig. 3d. And the right inset of Fig. 3d is a high-resolution TEM (HRTEM) image from the red circle in Fig. 3d. The spacing between adjacent lattice fringes in the portion of ZnO Fls is about 0.26 nm, which is due to the d spacing of the (0 0 2) plane, indicating the [0 0 1] direction (c axis) being the preferential growth direction of ZnO Fls. On the other hand, as to the nanoparticle of the heterodimer, lattice fringes with interplanar spacing of 0.23 nm corresponding to the {1 1 1} planes of fcc Ag are observed. The results of XRD patterns and HRTEM confirm that metallic Ag loaded ZnO Fls can be prepared by photoreduction method.

Synthesizing ZnO flower superstructures usually requires the formation of aggregated ZnO nuclei in an initial homogeneous nucleation process [29]. In this process, a large number of ZnO growth units result in a burst in homogeneous nucleation forming aggregated ZnO nuclei. The ZnO crystals produced during the initial growth stage have crystalline grains and boundaries, which contain more defects than other regions and are not thermodynamically stable. The initial ZnO grain may grow along one growth direction, but the large number of growth units could lead to the growth from the defects. The crystal surfaces containing defects are likely to further reduce their energy via surface reconstruction, which provides active sites for secondary nucleation. Therefore, the ZnO flower structures form in the presence of abundant growth units.
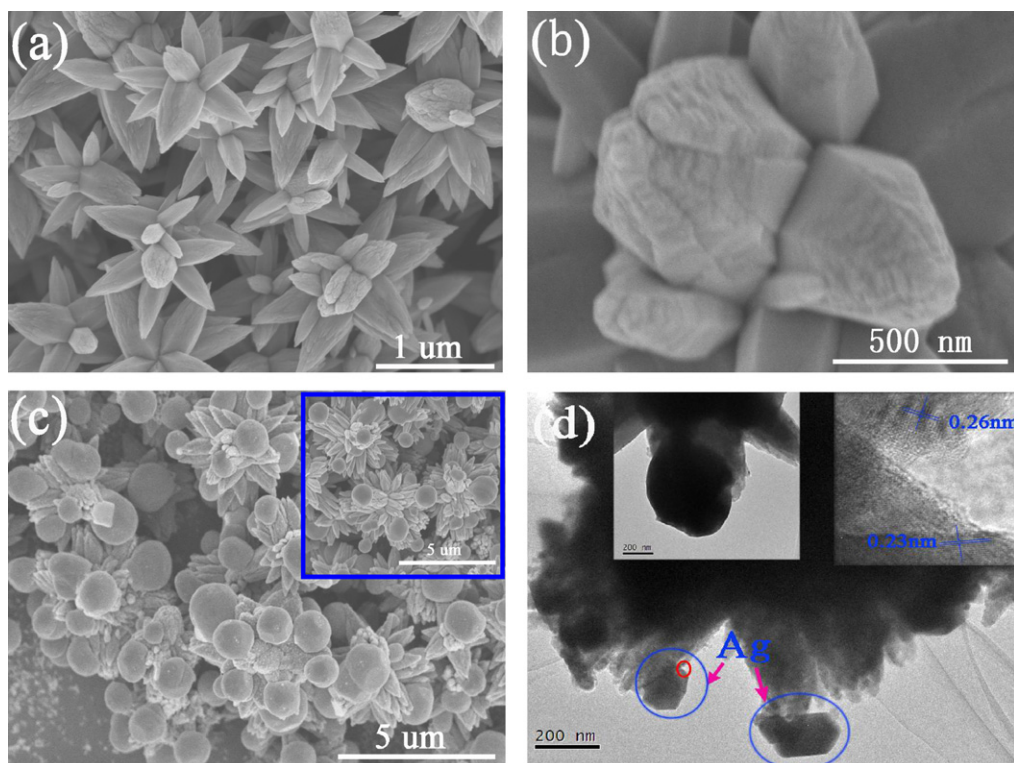

Fig. 3. FE-SEM images for the as-prepared samples: (a, b) ZnO Fls, (c) Ag/ZnO Fls, and (d) TEM image of Ag/ZnO Fls. (For interpretation of the references to color in text, the reader is referred to the web version of this article.)
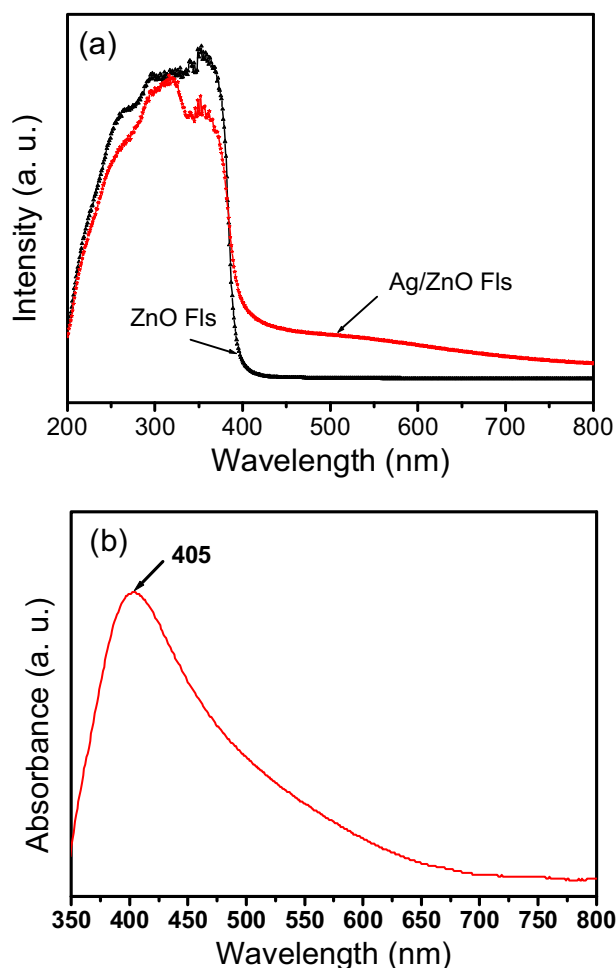
Fig. 4. (a) UV–vis diffuse reflectance spectra of ZnO Fls and Ag/ZnO Fls, and (b) UV–vis absorption spectra of Ag/ZnO Fls dispersed in water. (For interpretation of the references to color in this figure, the reader is referred to the web version of this article.)

3.2. Optical properties and surface characterization of Ag/ZnO Fls heterostructures

The diffuse reflectance spectra of ZnO Fls and Ag/ZnO Fls are demonstrated in Fig. 4a. The absorption edge at about 385 nm is assigned to the absorption of ZnO semiconductor. It shows a 10 nm red shift relative to other ZnO nanostructure [31], which might contribute to the enhanced photoactivities under visible light [27]. Compared to pure ZnO Fls, a broad absorption covers the range of 400–800 nm in the spectra of Ag/ZnO Fls, which should be attributed to the surface plasmon resonance effect of Ag.

Fig. 4b is a UV–vis absorption spectra of Ag/ZnO Fls dispersed in water. A plasmon absorption peak locates at 405 nm and red shifts compared to that of pure Ag NPs. When the Ag cluster is dispersed in the water, the λ_p is observed around 390 nm. It is evident that the red shift in the plasmon absorption is attributed to the formation of Ag/ZnO Fls nanocomposite. The plasmon absorption of silver λ_p is represented by the following equation [32]:

$$\lambda_p = \left[\frac{4\pi^2 c^2 m_{eff} \in_0}{N \cdot e^2} \right]^{1/2} \tag{1}$$

where m_{eff} is the effective mass of the free electron of metal and N is the electron density of the metal. From Eq. (1), it can be found that the plasmon absorption (λ_p) of Ag NPs is related to the electron density of metallic Ag. The electron density of the metallic Ag

decreases, then the plasmon absorption will increase accordingly. Herein, the red shift of the plasmon peak of Ag NPs suggests that the electron density of Ag decreases. The decrease in electron density of the Ag nanocrystals is because of the transfer of electrons from the Ag NPs to the ZnO Fls via ZnO—O···Ag bonds. It is known that the work function of ZnO (5.2 eV) is larger than that of Ag (4.26 eV), implying that the electrons will migrate from silver to the conduction band (CB) of ZnO to achieve the Fermi level equilibration when they get into contact [2].

The surface structures of the as-prepared ZnO Fls and Ag/ZnO Fls are investigated using XPS analysis. In Fig. 5a, all of the peaks on the curve of Ag/ZnO Fls are ascribed to Zn, Ag, O, and C elements and no peaks of other elements are observed, but there is no Ag peak for pure ZnO Fls. The presence of C is mainly from pump oil due to vacuum treatment before the XPS test [33]. Thus, the ZnO Fls is composed only with two elements, Zn, O, and Ag/ZnO Fls is formed by Zn, O, and Ag. The results are in good agreement with XRD and TEM as described above. Fig. 5b and c depicts the high-resolution spectrum for Zn, O and Ag species, respectively. It can be found that compared to ZnO Fls, there are positive shifts of Zn and O binding energy in Ag/ZnO Fls. In Fig. 5d, the O1s profile is asymmetric and can be fitted to two symmetrical peaks centered at 530.3 and 531.8 eV for Ag/ZnO Fls indicating that there are two different O species in the sample [13]. The higher binding energy component is usually associated with the chemically absorbed oxygen on the surface of ZnO Fls. The component near 530.3 eV is attributed to the lattice oxygen of ZnO Fls. In addition, no peak is present at the binding energy of about 529.0 eV, which is due to O in Ag_2O [34]. This suggests that the presence of silver is metallic. Interestingly, in Fig. 5e, the binding energies of Ag $3d_{5/2}$ and Ag $3d_{3/2}$ for Ag/ZnO Fls is at 367.6 and 373.6 eV, which shift remarkably to lower binding energy relative to the corresponding values of the synthesized pure metallic Ag (the standard binding energies of Ag $3d_{5/2}$ and Ag $3d_{3/2}$ for bulk Ag are about 368 and 374.2 eV, respectively) [35]. For Ag/ZnO Fls, the positive shift of Zn, O and the negative shift of Ag are due to the interaction between Ag nanoparticle and ZnO Fls [33]. Since the work function of silver is smaller than that of ZnO, once the Ag nanoparticle and ZnO Fls attach together, electron transfer occurs from Ag to the conduction band (CB) of ZnO nanocrystal. Thus, a new Fermi energy level in Ag/ZnO Fls is formed, resulting in the higher valence of Ag. These processes are described as Scheme 1. The binding energy of monovalent Ag is lower than that of zerovalent Ag [36], therefore, in our work, the binding energies of Ag $3d_{5/2}$ and Ag $3d_{3/2}$ shift to the lower ones in Ag/ZnO Fls.

3.3. Photoelectrochemical properties of Ag/ZnO Fl heterostructures

To further investigate the photo-induced behaviors and photo-electrochemical properties, the transient photocurrent responses of ZnO Fls and Ag/ZnO Fls were measured via the on–off illumination with visible light at 0.8 V vs Ag/AgCl. Several representative traces are described in Fig. 6 for comparing transient photocurrent responses of the different samples. It can be seen from Fig. 6 that Ag/ZnO Fls show much bigger photocurrent than the other. This indicates that under visible-light irradiation, there are many photo-induced electrons at the Ag surface due to separation of plasmon-induced electron–hole pairs at the interface of Ag and ZnO Fls, where the electrons transfer to ZnO Fls and ITO, while holes move to Ag surface and could be trapped or captured by RhB in the electrolyte. And it is not surprising that ZnO Fls exhibit very weak photocurrent because of their big band gaps. Additionally, a continuous decrease with time can be observed after the photocurrent reaches the summit. The photocurrent decay suggests that recombination processes are occurring. This process is that the holes may accumulate at the surface and recombine with electrons
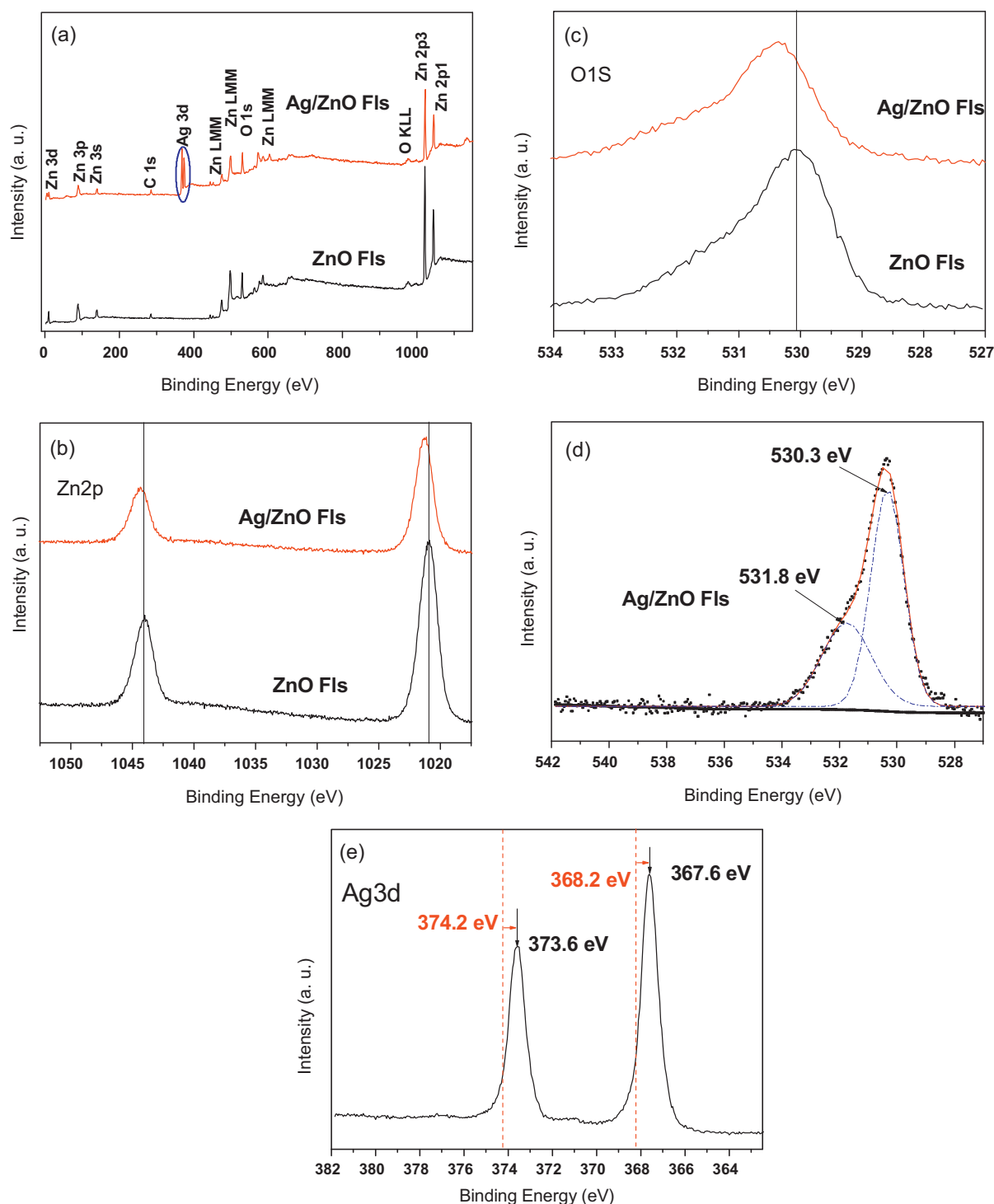
Fig. 5. XPS spectra of the as-prepared ZnO Fls and Ag/ZnO Fls: (a) XPS full spectra of the samples, (b) Zn 2p spectra, (c) O 1s spectra, (d) fit spectra of O 1s for Ag/ZnO Fls, and (e) Ag 3d spectra. (For interpretation of the references to color in this figure, the reader is referred to the web version of this article.)

from ZnO conduction band. Another recombination process causing the decay of the photocurrent is that conduction band electrons start to react with photo-generated oxidized species in the electrolyte.

As shown in Fig. 6, the transient photocurrent shows a slow response when the light is switched on. The electrons trapped in the surface defects of ZnO Fls are responsible for the slow photocurrent response [37]. The electrons trapped in the shallow surface state, which locates below the conduction band edge of ZnO, are released and retrapped into deep surface state,

resulting in more difficult to release. The deep surface states usually locate in the middle of the band gap. The rate of photo-induced electrons trapped in deep surface states is much slower than that of photo-induced electrons trapped in shallow surface states. Thus, the photo-induced electrons first fill the shallow traps, and then the trapped electrons transfer progressively to the deep surface states. As a result, only a part of photo-induced electrons transport to ITO until the deep surface states are filled, that cause a slowly increased current response. By the way, the response is quick while the light is off. This indicates that most of the photo-induced electrons at the
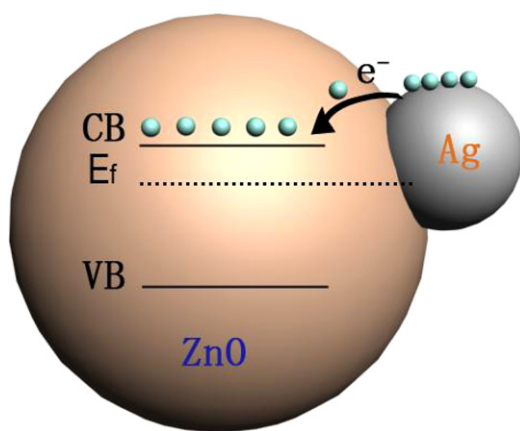
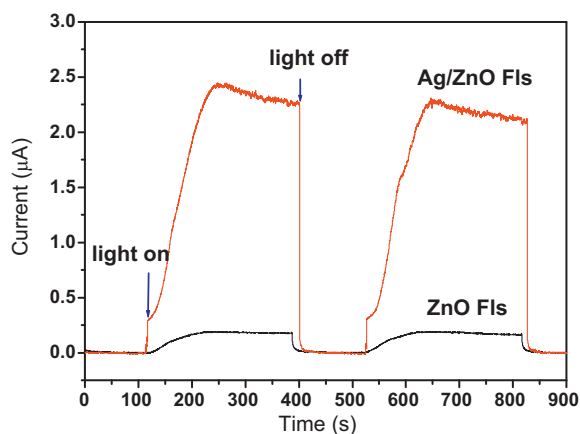**Scheme 1.** Electron transfer between the Ag metal and ZnO Fls.

Fig. 6. Photocurrent response with on–off light irradiation for ZnO Fls and Ag/ZnO Fls. (For interpretation of the references to color in this figure, the reader is referred to the web version of this article.)

Ag surface transfer to ZnO Fls, and then transport to ITO to produce photocurrent.

3.4. Photocatalytic activity and mechanism

The photocatalytic activity of the samples was evaluated by photodegradation of RhB aqueous solution under visible-light irradiation. The pure ZnO Fl samples also show visible-light photocatalytic activity as the heterostructures (as shown in Fig. 7a), which is due to the presence of chemisorbed RhB [38]. Chemisorbed RhB can be excited by visible-light, producing singlet and triplet excited states (RhB_{ads}^{*}). Electron transfer from excited dyes to the conduction band of semiconductor, and then the RhB* species are
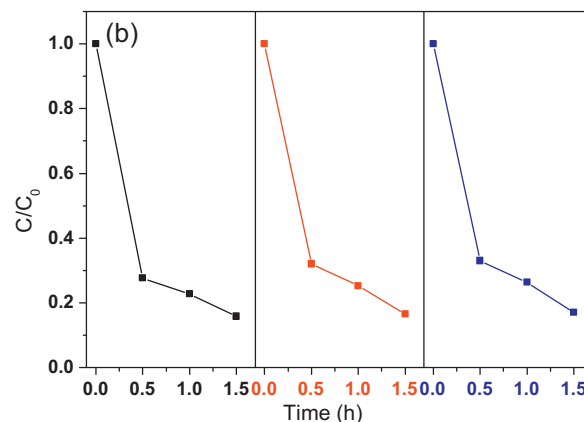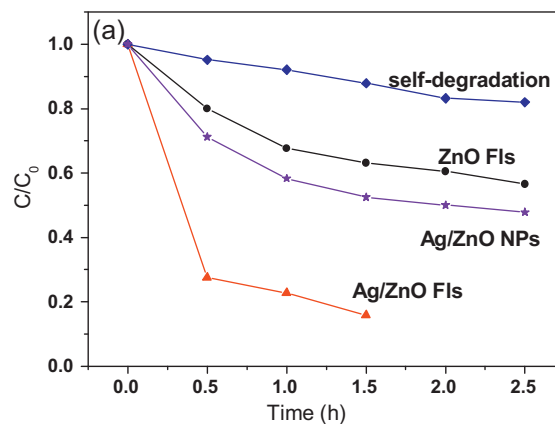

Fig. 7. (a) Photodegradation of RhB by ZnO Fls, Ag/ZnO NPs and Ag/ZnO Fls, and (b) photodegradation of RhB with Ag/ZnO Fls for three times. (For interpretation of the references to color in this figure, the reader is referred to the web version of this article.)

converted to radical $RhB_{ads}^{\bullet+}$. After several energy transfer processes, the hydroxyl radicals ($^{\bullet}OH$) are generated. Consequently, the degradation of RhB can also carry out for pure ZnO using visible-light.

However, as presented in Fig. 7a, the photocatalytic efficiency of Ag loaded samples is higher than that of pure ZnO Fls. And it also exhibits that the photodegradation rate of Ag/ZnO Fls is much higher compared with Ag/ZnO NPs, because the ZnO Fls have a larger areal proportion of exposed (0 0 1) faces, which are photocatalytic active crystal faces. Moreover, it is shown in Fig. 7b that the catalysts of Ag/ZnO Fls are stable and the decrease of photocatalytic efficiency is negligible after reusing for three times. In order to demonstrate the stability of photocatalysts, the XPS spectra of the Ag/ZnO Fls after photodegradation (denoted RhB-Ag/ZnO Fls) were recorded (Fig. 8). The notable shift does not occur for RhB-Ag/ZnO
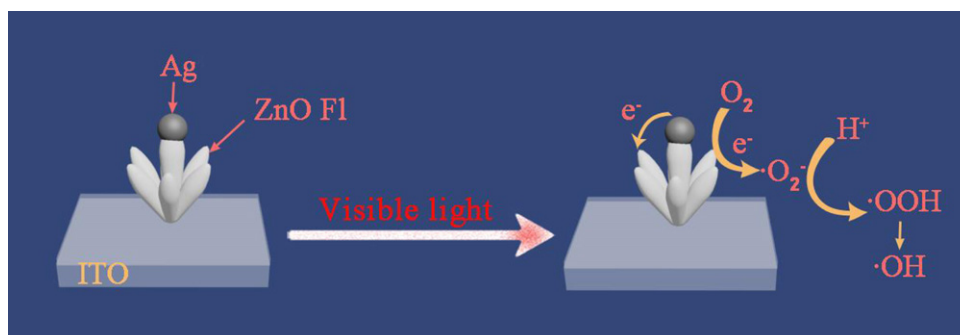
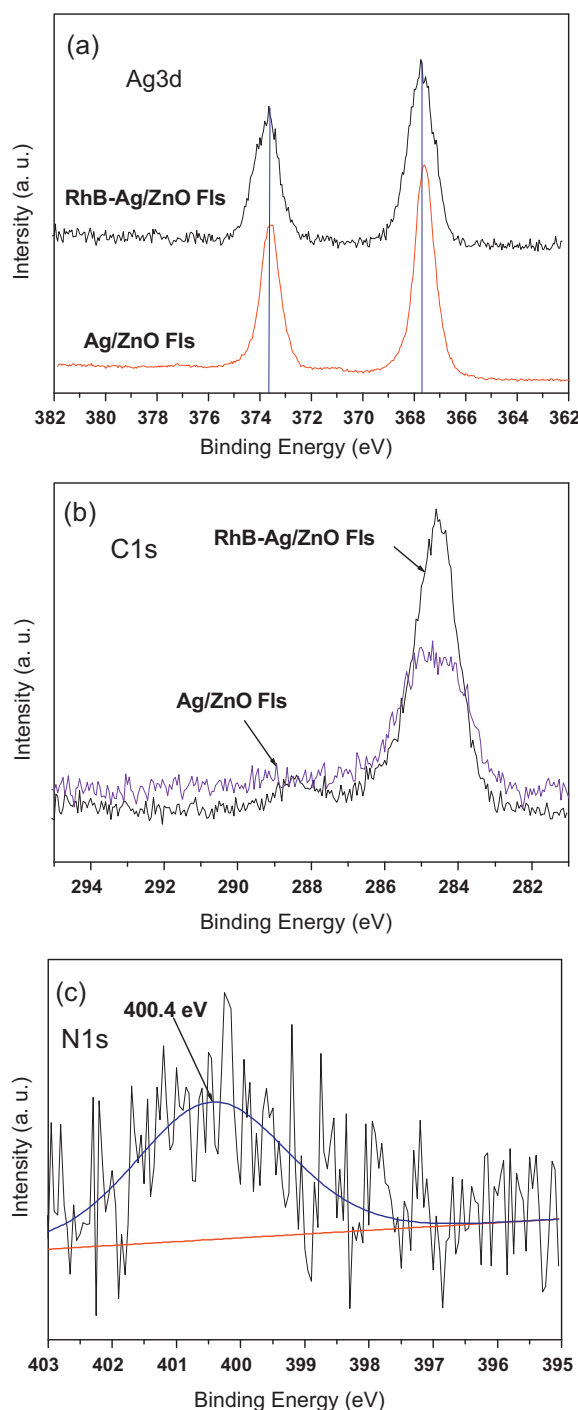**Scheme 2.** Schematic photocatalytic mechanism of Ag/ZnO Fls.

Fig. 8. XPS spectra for Ag/ZnO Fls after photocatalytic reaction: (a) Ag 3d spectra, (b) C 1s spectra, and (c) N 1s spectra. (For interpretation of the references to color in this figure, the reader is referred to the web version of this article.)

Fls compared with Ag/ZnO Fls, indicating that samples retain stable after photoreaction (Fig. 8a). But the intensity of C 1s peak is enhanced (Fig. 8b) and the N 1s peak is found in Fig. 8c, suggesting that the RhB were adsorbed on the surface of photocatalysts during the photodegradation process. These results confirm the photocatalytic mechanism for pure ZnO Fls under visible-light illumination.

The photocatalytic process under visible-light irradiation for Ag/ZnO Fls can be understood by the following suggested mechanism (as shown in Scheme 2). Under visible-light irradiation, photo-induced electron–hole pairs are generated in Ag NPs due to surface plasmon resonance. The photo-induced electrons transfer
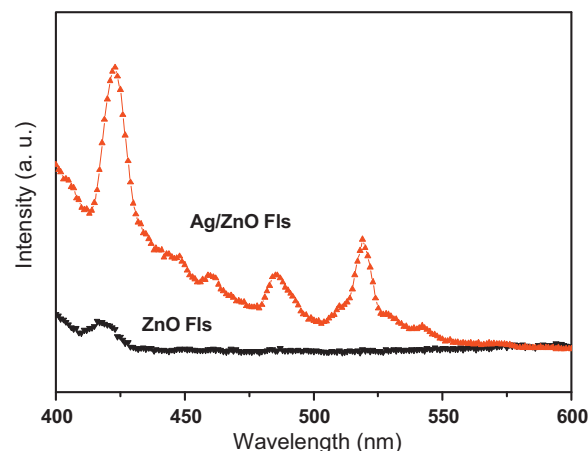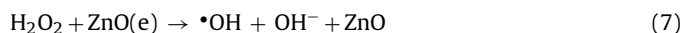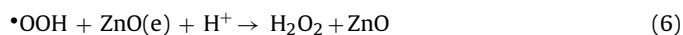

Fig. 9. PL spectra of ZnO Fls and Ag/ZnO Fls excited by 390 nm. (For interpretation of the references to color in this figure, the reader is referred to the web version of this article.)

from Ag NPs to ZnO conduction band, and the injected electrons are scavenged by adsorbed oxygen molecules to yield superoxide radical anions, $^{\bullet}O_2^-$. The radical anions can combine with H^+ to form $^{\bullet}OOH$, and $^{\bullet}OOH$ radicals and the trapped electrons combine to produce H_2O_2, finally forming $^{\bullet}OH$ radicals. Photodegradation of RhB can subsequently take place through $^{\bullet}OH$ radicals attacking the RhB molecules.

The major reaction steps in this plasmonic photocatalytic mechanism under visible-light irradiation can be formulated as Eqs. (2)–(8).

$$Ag + h\upsilon \rightarrow Ag* \tag{2}$$

$$Ag* + ZnO \rightarrow Ag^{\bullet+} + ZnO(e) \tag{3}$$

$$ZnO(e) + O_2 \rightarrow ZnO + {}^{\bullet}O_2^- \tag{4}$$

$${}^{\bullet}O_2^- + H^+ \rightarrow {}^{\bullet}OOH \tag{5}$$

$${}^{\bullet}OOH + ZnO(e) + H^+ \rightarrow H_2O_2 + ZnO \tag{6}$$

$$H_2O_2 + ZnO(e) \rightarrow {}^{\bullet}OH + OH^- + ZnO \tag{7}$$

$$RhB + {}^{\bullet}OH(or {}^{\bullet}OOH) \rightarrow degraded products \tag{8}$$

On the basis of the above discussion, it is concluded that Ag particles on the surface of ZnO Fls serve as electron sources (Eq. (2)) for degradation of RhB and ZnO Fls act as a media for the electrons transfer (Eq. (3)). Under visible-light irradiation, Ag can provide photo-induced electron via surface plasmon resonance. Consequentially, it is reasonable that the Ag/ZnO Fls heterostructure exhibit the higher catalytic activity in our system.

The PL technique is useful for understanding the surface processes in photocatalysis and confirming the photocatalytic mechanism. Since PL spectrum is an effective way to study the electronic structure, optical and photochemical properties of semiconductor materials, by which information such as surface oxygen vacancies and defects, as well as the efficiency of charge carrier trapping, immigration and transfer can be obtained [39]. Fig. 9 shows the PL spectrum of ZnO Fls and Ag/ZnO Fls, which were excited by 390 nm. An emission peak at about 420 nm is observed for both samples. This is due to the $^{\bullet}OH$ radicals, which could result in the degradation and mineralization of organic pollutant, and the PL intensity is proportional to the amount of $^{\bullet}OH$ generated at the water/catalyst interface [37]. So it can be found that there are more $^{\bullet}OH$ generated at the water/Ag/ZnO Fls interface, and the degradation efficiency will be enhanced. Additionally, two emission peaks centered at about 486 and 520 nm are observed only for Ag/ZnO Fls.

The two emission peaks result from the recombination of photo-induced electron and oxygen vacancies [40]. It suggests that few electrons are excited in the surface of ZnO Fls, because the excited energy is not much higher than the band gap energy of the catalyst, which can obtain from the diffuse reflectance spectra, but the photo-induced electrons can be formed in Ag NPs attribute to surface plasmon resonance. The results of the PL spectra further confirm that $^{\bullet}$OH species indeed participate in photodegradation, and the suggested mechanism is correct.

4. Conclusions

Ag/ZnO Fl heterostructures with higher photocatalytic performances were successfully prepared through a facile photoreduction method. It is found that the addition of Ag^{+} results in the formation of zerovalent metallic and the ZnO Fls are cone-like building blocks. The presence of Ag NPs promoting the absorption of visible-light attributes to the surface plasmon resonance. The binding energy of the three elements, Ag, Zn and O for the Ag/ZnO Fls samples shifts remarkably compared with pure metallic Ag and ZnO Fls, and this is because of the interaction between Ag and ZnO Fls. The transient photocurrent responses indicate that there are more photo-induced electrons on the surface of Ag/ZnO Fls under visible-light irradiation. After several energy transfer processes, the active photocatalytic species, hydroxyl radicals ($^{\bullet}$OH), are produced. These active species will result in the degradation of RhB. Therefore, the as-prepared Ag/ZnO Fls exhibit a higher visible-light driven photocatalytic activity. The photocatalytic mechanism is confirmed with PL spectra. Additionally, the Ag/ZnO Fl heterostructures could be applied for solar cells, gas sensors, and other devices.

Acknowledgements

References

[1] M.R. Hoffmann, S.T. Martin, W. Choi, D.W. Bahnemann, Chemical Reviews 95 (1995) 69–96.
[2] D.D. Lin, H. Wu, R. Zhang, W. Pan, Chemistry of Materials 21 (2009) 3479–3484.
[3] H. Tong, S. Ouyang, Y. Bi, N. Umezawa, M. Oshikiri, J.H. Ye, Advanced Materials 24 (2012) 229–251.
[4] Y.K. Su, S.M. Peng, L.W. Ji, C.Z. Wu, W.B. Cheng, C.H. Liu, Langmuir 26 (2010) 603–606.
[5] J.T. Tian, L.J. Chen, Y.S. Yin, X. Wang, J.H. Dai, Z.B. Zhu, X.Y. Liu, P.W. Wu, Surface and Coatings Technology 204 (2009) 205–214.
[6] O. Akhavan, ACS Nano 4 (2010) 4174–4180.
[7] N. Kislov, J. Lahiri, H. Verma, D.Y. Goswami, E. Stefanakos, M. Batzill, Langmuir 25 (2009) 3310–3315.
[8] X.Y. Yang, A. Wolcott, G.M. Wang, A. Sobo, R.C. Fitzmorris, F. Qian, J.Z. Zhang, Y. Li, Nano Letters 9 (2009) 2331–2336.
[9] P. Li, Z. Wei, T. Wu, Q. Peng, Y.D. Li, Journal of the American Chemical Society 133 (2011) 5660–5663.
[10] Y.Q. Qu, R. Cheng, Q. Su, X.F. Duan, Journal of the American Chemical Society 133 (2011) 16730–16733.
[11] Z.G. Xiong, J.Z. Ma, W.J. Ng, T.D. Waite, X.S. Zhao, Water Research 45 (2011) 2095–2103.
[12] S.W. Lama, K. Chiang, T.M. Lim, R. Amal, G.K.-C. Low, Applied Catalysis B 55 (2005) 123–132.
[13] C.A. Lin, D.S. Tsai, C.Y. Chen, J.H. He, Nanoscale 3 (2011) 1195–1199.
[14] K. Awazu, M. Fujimaki, C. Rockstuhl, J. Tominaga, H. Murakami, Y. Ohki, N. Yoshida, T. Watanabe, Journal of the American Chemical Society 130 (2008) 1676–1680.
[15] X. Chen, Z. Zheng, X. Ke, E. Jaatinen, T. Xie, D. Wang, C. Guo, J. Zhao, H. Zhu, Green Chemistry 12 (2010) 414–419.
[16] M.S. Zhu, P.L. Chen, M.H. Liu, ASC Nano 5 (2011) 4529–4536.
[17] T.S. Wu, K.X. Wang, G.D. Li, S.Y. Sun, J. Sun, J.S. Chen, ACS Applied Materials and Interfaces 2 (2010) 544–550.
[18] M. Rycenga, C.M. Cobley, J. Zeng, W.Y. Li, C.H. Moran, Q. Zhang, D. Qin, Y.N. Xia, Chemical Reviews 111 (2011) 3669–3712.
[19] F. Li, X.Q. Liu, Q.H. Qin, J.F. Wu, Z. Li, X.T. Huang, Crystal Research and Technology 44 (2009) 1249–1254.
[20] W. Song, Y.F. Wang, H.L. Hu, B. Zhao, Journal of Raman Spectroscopy 38 (2007) 1320–1325.
[21] Y.H. Zheng, C.Q. Chen, Y.Y. Zhan, X.Y. Lin, Q. Zheng, K.M. Wei, J.F. Zhu, Journal of Physical Chemistry C 112 (2008) 10773–10777.
[22] Y. Zhang, Z.Y. Zhang, B.X. Lin, Z.X. Fu, J. Xu, Journal of Physical Chemistry B 109 (2005) 19200–19203.
[23] H. Kim, H.H. Park, A.S. Reddy, H.H. Park, S.Y. Choi, Physical Status Solidi A 205 (2008) 2392–2395.
[24] D. Guin, S.V. Manorama, J.N.L. Latha, S. Singh, Journal of Physical Chemistry C 111 (2007) 13393–13397.
[25] A.M. Jones, S. Garg, D. He, A.N. Pham, T.D. Waite, Environmental Science and Technology 45 (2011) 1428–1434.
[26] H. Tran, J. Scott, K. Chiang, R. Amal, Journal of Photochemistry and Photobiology A 183 (2006) 41–52.
[27] H. Zhang, G. Wang, D. Chen, X.J. Lv, J.H. Li, Chemistry of Materials 20 (2008) 6543–6549.
[28] A. Takai, P.V. Kamat, ACS Nano 5 (2011) 7369–7376.
[29] S. Cho, J.W. Jang, J.S. Lee, K.H. Lee, Langmuir 26 (2010) 14255–14262.
[30] G.I.N. Waterhouse, G.A. Bowmaker, J.B. Metson, Physical Chemistry Chemical Physics 3 (2001) 3838–3845.
[31] C.Q. Chen, Y.H. Zheng, Y.Y. Zhan, X.Y. Lin, Q. Zheng, K.M. Wei, Dalton Transactions 40 (2011) 9566–9570.
[32] T. Hirakawa, P.V. Kamat, Journal of the American Chemical Society 127 (2005) 3928–3934.
[33] Y.H. Zheng, L.R. Zheng, Y.Y. Zhan, X.Y. Lin, Q. Zheng, K.M. Wei, Inorganic Chemistry 46 (2007) 6980–6986.
[34] J.F. Weaver, G.B. Hoflund, Chemistry of Materials 6 (1994) 1693–1699.
[35] C.D. Gu, C. Cheng, H.Y. Huang, T.L. Wong, N. Wang, T.Y. Zhang, Crystal Growth and Design 9 (2009) 3278–3285.
[36] J.F. Moudler, W.F. Stickle, P.E. Sobol, K.D. Bomben, Handbook of X-ray Photo-electron Spectroscopy, Perkin-Elmer, Eden Prairie, MN, 1992.
[37] J.G. Yu, G.P. Dai, B.B. Huang, Journal of Physical Chemistry C 113 (2009) 16394–16401.
[38] S. Horikoshi, A. Saitou, H. Hidaka, N. Serpone, Environmental Science and Technology 37 (2003) 5813–5822.
[39] L.Q. Jing, Y.H. Qu, B.Q. Wang, S.D. Li, B.J. Jiang, L.B. Yang, W. Fu, H.G. Fu, J.Z. Sun, Solar Energy Materials and Solar Cells 90 (2006) 1773–1787.
[40] A.B. Djurišić, A.M.C. Ng, X.Y. Chen, Progress in Quantum Electronics 34 (2010) 191–259.